



OPEN

SUBJECT AREAS:

SYNTHESIS AND  
PROCESSINGTWO-DIMENSIONAL  
MATERIALS

# Preparing two-dimensional microporous carbon from Pistachio nutshell with high areal capacitance as supercapacitor materials

Received  
23 April 2014Accepted  
16 June 2014Published  
2 July 2014

Correspondence and  
requests for materials  
should be addressed to  
Q.M.G. (qmgao@  
buaa.edu.cn)

Jiandong Xu, Qiuming Gao, Yunlu Zhang, Yanli Tan, Weiqian Tian, Lihua Zhu &amp; Lei Jiang

Key Laboratory of Bio-inspired Smart Interfacial Science and Technology of Ministry of Education, Beijing Key Laboratory of Bio-inspired Energy Materials and Devices, School of Chemistry and Environment, Beihang University, Beijing 100191, P. R. China.

**Two-dimensional (2D) porous carbon AC-SPN-3 possessing of amazing high micropore volume ratio of 83% and large surface area of about  $1069 \text{ m}^2 \text{ g}^{-1}$  is high-yield obtained by pyrolysis of natural waste Pistachio nutshells with KOH activation. The AC-SPN-3 has a curved 2D lamellar morphology with the thickness of each slice about 200 nm. The porous carbon is consists of highly interconnected uniform pores with the median pore diameter of about 0.76 nm, which could potentially improve the performance by maximizing the electrode surface area accessible to the typical electrolyte ions (such as  $\text{TEA}^+$ , diameter =  $\sim 0.68 \text{ nm}$ ). Electrochemical analyses show that AC-SPN-3 has significantly large areal capacitance of  $29.3/20.1 \mu\text{F cm}^{-2}$  and high energy density of  $10/39 \text{ Wh kg}^{-1}$  at power of  $52/286 \text{ kW kg}^{-1}$  in 6 M KOH aqueous electrolyte and 1 M TEABF<sub>4</sub> in EC-DEC (1 : 1) organic electrolyte system, respectively.**

Electrochemical capacitors (EDLC, known as ultracapacitors or supercapacitors) based on electrical double layer charge accumulation hold promise for a wide range of applications, including portable electric equipments, uninterruptable power sources, medical devices, load leveling and hybrid electric vehicles, and so forth<sup>1,2</sup>. Carbonaceous materials are the most common supercapacitor electrode active substances. The electrochemical performance of supercapacitors is highly determined by the adopted electrode materials with a rational design of the pore structure and morphology. There have been intensively investigated for supercapacitor electrode application such as activated carbons<sup>3</sup>, templated carbons<sup>4</sup>, carbon nanofibers<sup>5</sup>, carbon nanotubes<sup>6</sup>, carbide-derived carbons<sup>7</sup> and graphenes<sup>8–10</sup>. Several interesting synthetic routes have been found to obtain the high quality carbons, including carbonization of organic/polymeric precursors<sup>11–13</sup>, chemical vapor deposition<sup>14–19</sup>, excimer laser ablation of graphitic targets<sup>20–22</sup>, arc discharge syntheses<sup>23,24</sup>, sputtering/plasma based syntheses<sup>25,26</sup>, chemical methods, etc<sup>27,28</sup>. However, those methods have obvious shortages. For example, carbide-derived carbon (CDC) method is effective to prepare the high quality porous carbons where the carbons with high microporosity produced by extraction of other elements, such as Fe from iron carbide. Based on the equation of  $C/A = \epsilon_r \epsilon_0 / d$ , where C is the specific capacitance per weight, A is the specific surface area of the electrode, and  $\epsilon_r$  and  $\epsilon_0$  is the dielectric constant of the electrolyte and vacuum, respectively, the desolvated electrolyte ions derived from spatial restriction by the micropores were able to enhance the specific capacitance (C/A), since the desolvated electrolyte ions may approach the electrode surface more closely, decreasing the thickness d of the EDLC. In order for the chlorination reaction to proceed, highly corrosive HCl etc gases usually used and they were transported to the carbide/carbon interfaces and metals and metalloids were removed as chlorides, so the safety issues of the preparation process worth extra attention<sup>29,30</sup>.

Bio-inspired design strategies are powerful to prepare the medical materials and other functional materials<sup>31–34</sup>. The natural wastes such as nutshell, fruit kernel, leaf, straw and so forth mainly containing celluloses, hemicelluloses and lignin biopolymers are widely utilized as feedstock for the activated carbons, and one could get value-add produces for diverse and growing carbon-based applications. It was reported that the cation and/or anion with large sizes limit the utilizations of conventional porous activated carbon electrodes since the ions either literally do not fit into pores or become diffusion limited at the required scan rates<sup>35,36</sup>. In order to enhance the quality of the activated carbons, the porous carbons were usually treated by pyrolyzing the waste materials with some chemical or physical additives as agents for further activation. Physical activation (*i.e.*, by steam or



CO<sub>2</sub>) was found able to significantly develop pores in wide range of diameters<sup>37</sup>. Chemical activation (such as by KOH, HNO<sub>3</sub> or H<sub>3</sub>PO<sub>4</sub>) could not only form micropores<sup>38–41</sup>, but also produce surface functional groups<sup>39,42–44</sup>. Chemical activation is usually a lower temperature process, resulting in lower energy cost and shorter time with higher carbon yield than that used in physical activation. Recently, an outstanding specific capacitance of 200–300 F g<sup>-1</sup> in organic electrolyte or ionic liquid was reported by employing improved activation carbon electrode with tailored pore size distribution<sup>45,46</sup>. Because of an intrinsically high fraction of microporosity, which limits the pore accessibility of the electrolyte ions at high scan rates<sup>34</sup>, the powers of those carbons remain limited. We all know that the key to achieving high power in porous electrodes is to reduce the ion transport time ( $\tau$ ), which can be expressed by the equation  $\tau = l^2/d$ , where  $l$  is the ion transport length and  $d$  is the ion transport coefficient<sup>47</sup>. The materials with open low-dimensional (1D or 2D) morphology could possess an intrinsic advantage over the particulate materials since the ion transport length is significantly shortened in the thin dimension<sup>48,49</sup>. Here, we report the preparation of 2D microporous carbons by a new bio-inspired technique of pyrolysis and KOH activation of natural waste Pistachio nutshell. The method is facile and safety, possessing of high product yield (62.3 wt.%) and easy for mass production. The microporous carbon products have high performance using as the EDLC electrode active materials.

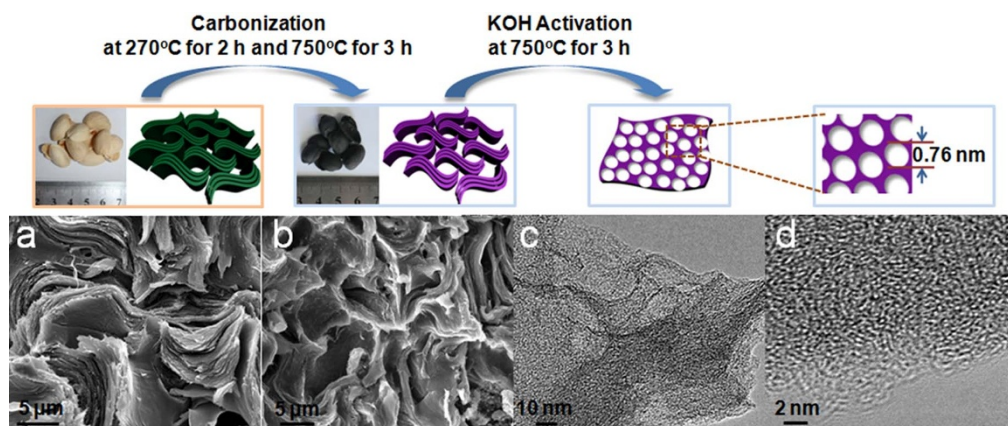
## Results

The Pistachio nutshell was pyrolyzed at 750°C (denoted as C-SPN) and activated with KOH labeled as AC-SPN-X, where X refers to the mass ratio between KOH and carbon materials. Figure 1 and Figure S1 show the scanning electron microscopy (SEM) images of natural Pistachio shell and C-SPN with different magnification times. Both natural Pistachio shell and C-SPN possess curved 2D lamellar structures and certain shrinkage could be observed for C-SPN (Fig. 1b), indicating that the C-SPN preserves a wealth of natural plant features of the Pistachio nutshell. The thickness of each slice of C-SPN is approximately 200 nm based on the SEM observation (insert in Fig. S1b). The surface of C-SPN is flat and smooth (Fig. S2 a and b). The rough surface with many pores could be observed after the activation (Fig. S2 c–h). The damages became more apparent when the mass ratios of KOH/C increased from 1 to 5. Figure 1 c and d shows the high resolution transmission electron microscopy (HRTEM) images of AC-SPN-3 that further highlights the porous structure. The AC-SPN-3 constructed of amorphous and graphitized carbons (Fig. S3)

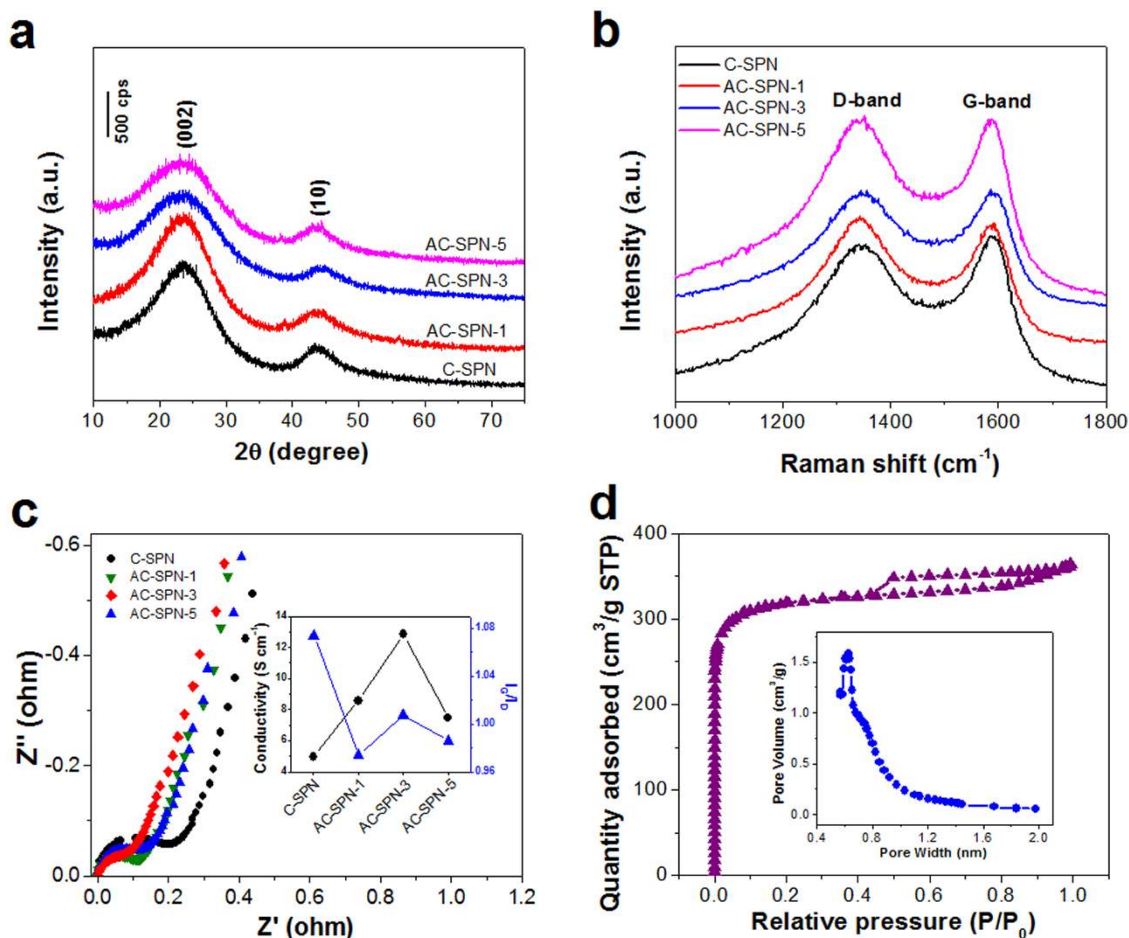
has highly interconnected pores with the pore size of about 0.5–1 nm (Fig. 1 c and d).

Figure 2a shows the X-ray diffraction (XRD) patterns of the C-SPN as well as AC-SPN-1, AC-SPN-3 and AC-SPN-5 porous carbon materials. All the samples have two broad diffraction peaks at around  $2\theta = 24^\circ$  and  $43^\circ$  in the XRD patterns, which are consistent with the graphitic carbon. The broad diffraction pattern at  $2\theta$  value of about  $24^\circ$  may be attributed to the (002) reflection of the graphitic-type lattice. The weak diffraction pattern at around  $43^\circ$  corresponds to a superposition of the (100) and (101) reflections of the graphitic-type lattice, *i.e.*, (10) reflection, indicating a limited degree of graphitization. The specific structure nature can be further elucidated by the Raman spectroscopy. In Figure 2b the peaks present at around 1320 cm<sup>-1</sup> (D-bands) are due to the breathing mode of  $\kappa$ -point phonons with A<sub>1g</sub> symmetry, corresponding to the disordered carbon or defective graphitic structures<sup>50,51</sup>. The peaks at around 1580 cm<sup>-1</sup> (G-bands) are assigned to the E<sub>2g</sub> phonon of sp<sup>2</sup> carbon atoms<sup>52,53</sup>, which are characteristic feature of the graphitic layers and correspond to the tangential vibration of the carbon atoms. Thus, the intensity ratios of these two peaks partially depend on the graphitization degrees<sup>54</sup>, and the higher value of  $I_G : I_D$  indicating higher electrical conductivity may be expected. Figure 2c shows the Nyquist plot for different carbon materials in 6 M KOH in the frequency range from 0.01 Hz to 0.1 mHz. The inset in Figure 2c shows the conductivities of the C-SPN and AC-SPN-X electrodes as well as the ratios of  $I_G/I_D$  from the Raman spectra for the C-SPN and AC-SPN-X samples. The Nyquist plots are composed of two distinct parts: one is semicircle part at high frequency with the corresponding value of the first intersection of the curve with the real axis indicates the internal resistance of the electrodes, and the other is linear part at low frequency corresponding to the diffusion process of the electrolyte ions onto the surface of the electrode in the system. After fitting the Nyquist plots with the typical circuit model, we can conclude that the electrode containing AC-SPN-3 possesses the highest conductivity of 12.8 C cm<sup>-1</sup> among those carbon electrodes (inset in Fig 2c). Besides, the  $I_G/I_D$  value of AC-SPN-3 is relatively high compared to that of AC-SPN-1 and AC-SPN-5 (inset in Fig 2c), indicating that the AC-SPN-3 sample has the most abundant graphitic layers among the activated samples even though the presence of disorder in the structure<sup>51</sup>.

The porosities of the AC-SPN-3 were examined by the N<sub>2</sub> sorption measurements (Fig. 2d) with the related textural parameters including Brunauer-Emmett-Teller (BET) specific surface areas ( $S_{BET}$ ), total pore volumes ( $V_t$ ), micropore volumes ( $V_{mi}$ ), pore diameters ( $D_{por}$ ) and the ratios of  $V_{mi}/V_t$  summarized in Table 1. For comparison, the



**Figure 1** | The simulation models as well as the SEM and HRTEM images of four characteristic states of the carbon representing the reaction process. (a), SEM image of the Pistachio nutshell, which has continuous, uniform and lamellar natural structure. (b), SEM image of the carbonized nutshell, which possesses curved 2D lamellar structure with certain shrinkage compared with that of the natural structure. The resultant porous carbon preserves a wealth of natural plant features of the Pistachio nutshell. And (c) and (d), HRTEM images with different magnification times highlight the porous structure of AC-SPN-3. The diameter of the pore is about 0.5–1 nm.



**Figure 2** | XRD, Raman patterns and BET tests. (a), XRD profiles for pristine activated carbon (C-SPN) as well as the samples activated with KOH at different ratios (AC-SPN-1, AC-SPN-3 and AC-SPN-5). (b), Raman spectra of the resultant pristine activated carbon and samples after KOH activation. (c), The Nyquist plot for the carbon electrode in 6 M KOH with the insert of the conductivities of the C-SPN and AC-SPN-X electrodes as well as the ratios of  $I_G/I_D$  from the Raman spectra for the C-SPN and AC-SPN-X samples. The AC-SPN-3 electrode possesses the highest conductivity of  $12.8 \text{ C cm}^{-1}$  among those carbon electrodes. And (d),  $\text{N}_2$  sorption isotherms of AC-SPN-3. Typical I curves was observed, indicating uniform microporous structure. The inset is pore size distribution, showing the main pore size of 0.76 nm.

textural parameters of the related typical porous carbons in the literatures are also listed in Table 1<sup>55–63</sup>. The total BET surface of the AC-SPN-3 sample is about  $1069 \text{ m}^2 \text{ g}^{-1}$ , which is parallel to that of the porous carbon CN2 ( $1061 \text{ m}^2 \text{ g}^{-1}$ ) prepared by the template method<sup>56</sup> and the porous carbons obtained by the CDC techniques where the carbide  $\text{Ti}_2\text{AlC}$  ( $1150 \text{ m}^2 \text{ g}^{-1}$ ) or  $\text{TiC}$  ( $1000\text{--}1600 \text{ m}^2 \text{ g}^{-1}$ ) was used as the precursor<sup>59</sup>. This high surface area is favorable for the

high performances of the AC-SPN-3 sample using as the supercapacitor electrode material. The total pore volume of AC-SPN-3 is  $0.51 \text{ cm}^3 \text{ g}^{-1}$  based on the  $\text{N}_2$  desorption curve analyses, which is in the middle level among the porous carbons prepared from the natural products or wastes. The AC-SPN-3 material has a uniform pore size distribution with the pore diameter of about 0.76 nm, based on the HK method, which is close to and a little larger than the diameter

**Table 1** | Comparison of pore parameters and specific capacitances of the porous carbons prepared by different methods

Sample	$S_{\text{BET}}$ [ $\text{m}^2/\text{g}$ ]	$V_1$ [ $\text{cm}^3/\text{g}$ ]	$V_{\text{mi}}$ [ $\text{cm}^3/\text{g}$ ]	$D_{\text{por}}$ [nm]	$V_{\text{mi}}/V_1$ [%]	Maximum capacitance [ $\text{F}/\text{m}^2$ ]	Method (or Material)	Reference
ACK-3	2009	1.00	0.82	0.59	82	-	Second activation	55
CN2	1061	0.68	0.36	3.1	53	0.11	Template	56
CNX-1	1803	0.93	0.74	3.10	80	0.08	Template	57
CS48A2	2737	1.43	0.81	2.40	57	0.07	Template	58
C-B <sub>4</sub> C	1850	-	-	1.25	-	<0.15	CDC	59
C-Ti <sub>2</sub> AlC	1150	-	-	2.25	-	<0.15	CDC	59
CNS-700	1340	1.08	0.53	-	60	0.07	Hemp	60
HPC-1	2157	2.26	0.77	4.18	34	0.09	Animal bone	61
AKO	1654	1.29	0.62	-	52	0.17	Argan seed shell	62
HFAC-2	1217	0.46	0.41	-	88	0.46	Egg white	63
AC-SPN-3	1069	0.51	0.42	0.76	83	0.293 (aqueous)/0.201 (organic)	Pistachio nutshell	Our work

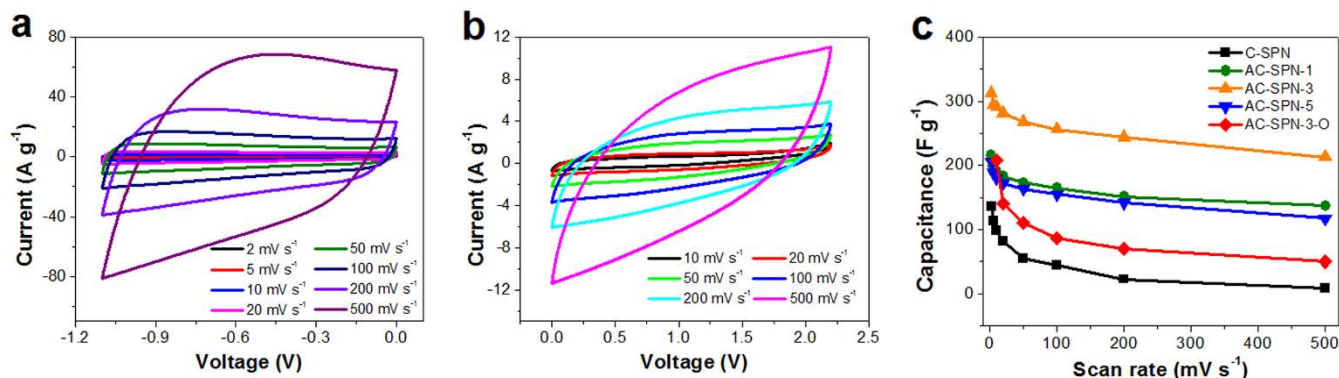


**Figure 3** | Electrochemical capacitive behaviors of the carbon samples. (a) and (b), CV measurements of AC-SPN-3 at different scan rates in 6 M KOH aqueous and 1 M TEABF<sub>4</sub> EC-DEC organic electrolyte systems, respectively. And (c), Specific capacitance measured at different scan rates, tested at 25 °C, for the C-SPN, AC-SPN-1, AC-SPN-3 and AC-SPN-5 in the aqueous and organic electrolyte systems.

of (CH<sub>3</sub>CH<sub>2</sub>)<sub>4</sub>N<sup>+</sup> (TEA<sup>+</sup>, 0.68 nm), a typical ion of the solute TEABF<sub>4</sub> for the organic electrolyte of supercapacitor. It should be mentioned that AC-SPN-3 possesses a high micropore ratio with the  $V_{mi}/V_t = 83%$ , which is much higher than that of the typical porous carbons prepared from the natural products or wastes, such as CNS-700 (60%, from Hemp<sup>60</sup>), HPC-1 (34%, from animal bone<sup>61</sup>), or AKO (52%, Argan seed shell<sup>62</sup>). Thus, high capacitor properties are anticipated for the AC-SPN-3 using as the electrode active material in the organic electrolyte system.

The electrochemical properties of the C-SPN as well as AC-SPN-1, AC-SPN-3 and AC-SPN-5 samples were investigated in 6 M KOH aqueous electrolyte system. Without activation the C-SPN cyclic voltammetry (CV) curves (Fig. S4a) are disorder due to the low ion transport properties. Much better CV curves could be found for the AC-SPN-1 and AC-SPN-5 samples (Fig. S4 b and c). Quasi-rectangular shape curves were observed from the CV data for AC-SPN-3 (Fig. 3a), indicating the best electrochemical property of AC-SPN-3 sample among the C-SPN and AC-SPN-X samples. 1 M tetraalkylammonium tetrafluoroborate (TAABF<sub>4</sub>) in EC-DEC (1 : 1) organic electrolyte system was chosen to investigate the behavior of the AC-SPN-3 sample, where tetramethylammonium tetrafluoroborate (TMABF<sub>4</sub>), tetraethylammonium tetrafluoroborate (TEABF<sub>4</sub>), tetrapropylammonium tetrafluoroborate (TPABF<sub>4</sub>) and tetrabutylammonium tetrafluoroborate (TBABF<sub>4</sub>) possessing of the effective cationic size of TMA<sup>+</sup> 0.50 nm, TEA<sup>+</sup> 0.68 nm, TPA<sup>+</sup> 0.92 nm and TBA<sup>+</sup> 1.11 nm was used as the solute, respectively. The CV result of AC-SPN-3 in the TEABF<sub>4</sub> electrolyte system (Fig. 3b) was obviously higher than that in the TMABF<sub>4</sub>, TPABF<sub>4</sub> and TBABF<sub>4</sub> electrolyte systems (Fig. S5). The effective cationic size of the TEA<sup>+</sup> ion (0.68 nm) is the closest to the median pore diameter (0.76 nm) of AC-SPN-3 among the TAA<sup>+</sup> ions. Thus, the obtained higher CV values of AC-SPN-3 in the TEABF<sub>4</sub> system may be due to the desolvated TEA<sup>+</sup> ions approach the AC-SPN-3 electrode surface more closely than the other TMA<sup>+</sup>, TPA<sup>+</sup> and TBA<sup>+</sup> ions, which may result in decrease of the thickness *d* of the EDLC. Those experimental results and related structure parameters (Table S1) further confirm the fact that charge storage in pores comparable to the size of desolvated electrolyte ions can lead to enhanced capacitive value<sup>59</sup>. The quasi-rectangular shape CV curves still keep for AC-SPN-3 tested at 25 °C in both aqueous (Fig. 3a) and organic (Fig. 3b) electrolyte systems even at a high scan rate of 500 mV s<sup>-1</sup>, demonstrating an excellent ion transport behavior for AC-SPN-3. Figure 3c shows the specific capacitances of the C-SPN, AC-SPN-1, AC-SPN-3 and AC-SPN-5 in the aqueous electrolyte systems and that of AC-SPN-3 in the organic electrolyte system measured at different scan rates. It is clear that the specific capacitances decreased along with the increase of the scan rates.

The specific capacitances of the AC-SPN-3 demonstrate an amazing high values in both aqueous and organic electrolyte systems,

reached 313 and 215 F g<sup>-1</sup>, *i.e.* the surface area normalized capacitance of 29.3 and 20.1 μF cm<sup>-2</sup> at a current of 2 mV s<sup>-1</sup>, respectively. This result is apparently higher than that of the recently reported activated graphene (~6.9 μF cm<sup>-2</sup>)<sup>10</sup>, porous carbon from the template methods<sup>56–58</sup>, carbide-derived carbons (7 ~ 14 μF cm<sup>-2</sup>)<sup>7,59</sup> and most of porous carbons from the pyrolyses of the natural products or rests<sup>60–62</sup> (Table 1), even though the values are still lower than that of HFAC-2 (~46 μF cm<sup>-2</sup>) prepared from the expensive natural egg white<sup>63</sup>. The specific capacitances of the C-SPN and AC-SPN-3 samples were dropped slowly along with the increase of the scan rates. The specific capacitances of the AC-SPN-3 may still keep up to 213 and 137 F g<sup>-1</sup> at the high scan rate of 500 mV s<sup>-1</sup>, which was 68 and 64% of the specific capacitance at 2 mV s<sup>-1</sup> in the aqueous and organic electrolyte system, respectively. Compared to the samples without activation, the specific capacitance increased by 230% (the specific performance of the C-SPN is 136 F g<sup>-1</sup>) at the scan rate of 2 mV s<sup>-1</sup> in the aqueous electrolyte system. Obviously, the activation process improves the electrochemical performance of those carbon materials greatly.

The galvanostatic charge/discharge curves of AC-SPN-3 at different current densities and electrolyte systems are shown in Figure 4 a and b. The curves are highly linear and symmetrical, meaning that the AC-SPN-3 has excellent electrochemical reversibility and Coulombic efficiency. For AC-SPN-3 in aqueous electrolyte system (Fig. 4a), the IR drop is 0.03 V at a current density of 0.2 A g<sup>-1</sup>, and the specific capacitance is about 261 F g<sup>-1</sup>. While the IR drop enhances along with the increase of the current densities. The AC-SPN-3 possesses typical triangular shapes with a little galvanostatic discharge decrease caused by the inner resistance throughout the current range of 0.2–1.5 A g<sup>-1</sup>, indicating its excellent capacitive properties. The special capacitance of AC-SPN-3 is about 214, 180, 158, 132, 108 and 97 F g<sup>-1</sup> at the current density of 0.5, 1, 2, 3, 6 and 8 A g<sup>-1</sup>, respectively, in the organic electrolyte of TEABF<sub>4</sub> system (Fig. 4b). It can be clearly seen that the curves show triangular nature in the scan rates. When the current density increases, the specific capacitance value decreases because of the limited diffusion of the active ions on the electrode surface in the case of fast charging. Figure 4c shows the Ragone plots of the AC-SPN-1, AC-SPN-3 and AC-SPN-5 samples in the two-electrode configuration. The AC-SPN-3 has a high energy density of 10 Wh kg<sup>-1</sup> at the power of 52 kW kg<sup>-1</sup> in 6 M KOH electrolyte system. Much higher energy density of 39 Wh kg<sup>-1</sup> at the power of 286 kW kg<sup>-1</sup> was observed in the TEABF<sub>4</sub> electrolyte system. Likewise, the desolvated TEA<sup>+</sup> ions with the effective cationic size of 0.68 nm, similar to the median pore diameter (0.76 nm) of the AC-SPN-3, may approach the AC-SPN-3 electrode surface more closely (insert in Fig. 4c), decreasing the thickness *d* of the EDLC and leading to a higher special areal capacitance<sup>59</sup>. The obviously high electrochemical properties of the AC-SPN-3 is the result of the beneficial synergistic effects of the large number of highly interconnected

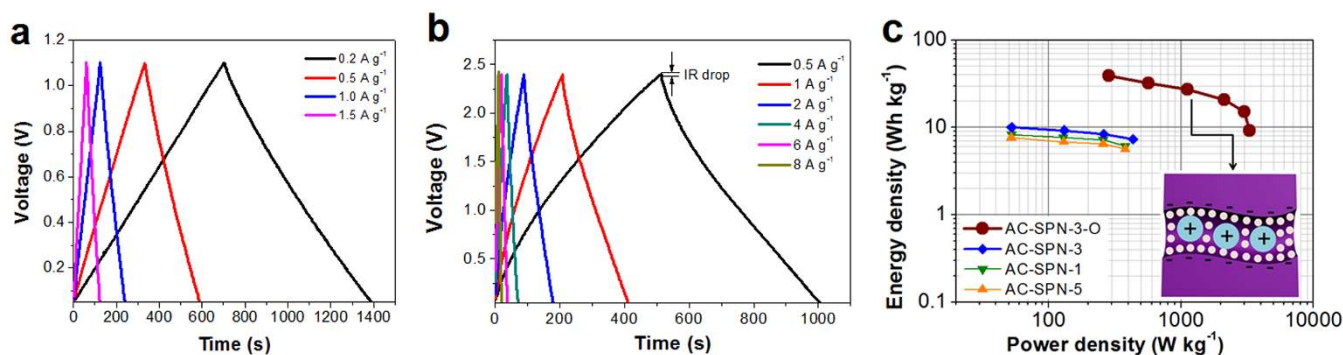


**Figure 4 | Electrochemical properties of the AC-SPN-3 sample.** (a) and (b), Galvanostatic charge-discharge profiles of AC-SPN-3 at different currents in 6 M KOH aqueous and 1 M TEABF<sub>4</sub> EC-DEC organic electrolyte systems. And (c), The Ragone plot of the carbon samples in the aqueous and organic electrolyte systems with the insert of the schematically drawing of the (CH<sub>3</sub>CH<sub>2</sub>)<sub>4</sub>N<sup>+</sup> ions residing in pores with diameter of about 0.76 nm. The desolvated electrolyte ions may approach the electrode surface more closely, decreasing the thickness *d* of the EDLC and leading to high special areal capacitances.

uniform micropores with suitable size and high surface areas and the abundant curved 2D lamellar graphitic layers with thin nanometer dimensions present in the carbon matrix.

## Discussions

Bio-inspired design strategy has been implemented to prepare the two-dimensional lamellar microporous carbon supercapacitor electrode active material with large surface area. The high quality material has been obtained by pyrolysis of natural waste Pistachio nutshells followed by KOH activation, the method is facile and safety, the yield is high, and scalability of the process is quite easy. The microporous carbon possesses a curved lamellar morphology inheritance of the natural plants feature in the scale of micron/nanometer. The material exhibits very high areal electrical double layer charge accumulation capacitances in both aqueous and organic electrolyte systems in comparison with those of currently reported activated graphene, porous carbon from template methods, carbide-derived carbons and most of porous carbons from the pyrolyses of the natural products or rests, due to the strong synergistic effects of the large number of highly interconnected uniform micropores with suitable size and high surface areas and the abundant curved 2D lamellar morphology with thin nanometer dimensions. This result is obviously valuable for the utilization of inexpensive, abundant and sustainable natural waste of Pistachio nutshell, *i.e.*, typically turn “waste” into wealth.

## Methods

**Materials preparation.** The Pistachio nutshell were collected in large quantity, thoroughly washed, clean and dried at 60°C in an oven. For synthesis of functional carbon, 15 g of the nutshell was heated in an alumina crucible at 270°C for 2 h and 750°C for 3 h in an argon atmosphere at a heating rate of 3°C min<sup>-1</sup>. After the calcinations, the obtained samples were washed with HF solution to remove the residual SiO<sub>2</sub> and consequently washed by water and dried. The resultant porous carbon was denoted as C-SPN.

The as-synthesized porous carbon of C-SPN (11 g) was further activated with KOH, which performed by heating the mixture of the carbon and KOH with the mass ratio of KOH/carbon of 1 : 1, 3 : 1 and 5 : 1, respectively. The mixture was placed in a tube furnace and then heated to the activation temperature of 750°C with a heating rate of 1.5°C min<sup>-1</sup> under argon atmosphere. Finally, the mixture was removed and washed several times with 20 vol.% hydrochloric acid at room temperature and then with sufficient deionized water. The resultant sample were dried at 100°C for 12 h. The sample after activation was labeled as AC-SPN-1, AC-SPN-3, and AC-SPN-5, respectively.

**Characterization.** The carbon samples were determined using X-ray diffractometry (Labx XRD-6000, Shimadzu, Japan) with Cu K $\alpha$  radiation (wavelengths  $\lambda$  = 0.15418 nm) in the range of 10°  $\leq$  2 $\theta$   $\leq$  70° (scan speed 3° min<sup>-1</sup> and scan step 0.02°) at room temperature. SEM images of the carbons were observed via scanning electron microscopy (SEM, Quanta-250 FEG, Holland) with 5 kV voltage and 10  $\mu$ A current and a working distance 8 ~ 10 mm. (HR)TEM observations were made at 200 kV on a JEOL JEM-2100F microscope with field-emission gun. Nitrogen isotherm at 77 K was obtained using a surface area and pore size analyzer (Micromeritics ASAP 2020).

The sample was degassed at 330°C for 12 h. The electrochemical measurement experiments were carried out on a CHI660e electrochemical work station (Shanghai Chenhua Instruments Co.) at room temperature. The working electrodes were prepared by loading a slurry containing 80 wt.% porous carbon (about 2.3 mg), 10 wt.% poly(vinylidene fluoride) (PVDF) (in N-methylpyrrolidone) and 10 wt.% acetylene black on a nickel foam. After the electrode materials were loaded, the working electrode was pressed and dried in vacuum at 80°C for 12 h. In a three-electrode system, the above loaded nickel foam as working electrode was investigated with a Pt counter electrode and Ag/AgCl reference electrode in 6 M KOH solution and 1 M TAABF<sub>4</sub> in EC-DEC (1 : 1) organic electrolyte as the electrolyte. The charge-discharge measurements were carried out using coin cells CR2032. A total of 2032 stainless steel coin cells with two symmetrical carbon electrodes separated by a porous polymeric separator were assembled with the aqueous and organic electrolytes. Electrochemical impedance spectroscopy (EIS) measurements were conducted for the working electrode in a frequency range of 0.01 Hz to 0.1 mHz. The EIS data were analyzed using Nyquist plots, which represent the real part (*Z'*) and imaginary part (*Z''*) of impedance.

- Conway, B. E. Electrochemical supercapacitors: scientific fundamentals and technological applications. *Kluwer Academic/Plenum: New York* 1999.
- Simon, P. & Gogotsi, Y. Materials for electrochemical capacitors. *Nat. Mater.* **7**, 845–854 (2008).
- Balducci, A. *et al.* High temperature carbon-carbon supercapacitor using ionic liquid as electrolyte. *J. Power Sources* **165**, 922–927 (2007).
- Lazzari, M., Soavi, F. & Mastragostino, M. Mesoporous carbon design for ionic liquid-based, double-layer supercapacitors. *Fuel Cells* **10**, 840–847 (2010).
- Xu, B., Wu, F., Chen, R., Gao, G., Chen, S. & Yang, Y. Mesoporous activated carbon fiber as electrode material for high-performance electrochemical double layer capacitors with ionic liquid electrolyte. *J. Power Sources* **195**, 2118–2124 (2010).
- Kang, Y. J. *et al.* All-solid-state flexible supercapacitors based on papers coated with carbon nanotubes and ionic-liquid-based gel electrolytes. *ACS Nano* **6**, 6400–6406 (2012).
- Largeot, C., Portet, C., Chmimola, J., Taberna, P. L., Gogotsi, Y. & Simon, P. Relation between the ion size and pore size for an electric double-layer capacitor. *J. Am. Chem. Soc.* **130**, 2730–2731 (2008).
- Stoller, M. D., Park, S., Zhu, Y., An, J. & Ruoff, R. S. Graphene-based ultracapacitors. *Nano Lett.* **8**, 3498–3502 (2008).
- Kim, T. Y. *et al.* High-performance supercapacitors based on poly(ionic liquid)-modified graphene electrodes. *ACS Nano* **5**, 436–442 (2011).
- Zhu, Y. *et al.* Carbon-based supercapacitors produced by activation of graphene. *Science* **332**, 1537–2541 (2011).
- Jagdale, P., Sharon, M., Kalita, G., Maldar, N. M. & Sharon, M. Carbon nanomaterial synthesis from polyethylene by chemical vapour deposition. *Adv. Mater. Phys. Chem.* **2**, 1–10 (2012).
- Shaikjee, A. & Coville, N. J. The role of the hydrocarbon source on the growth of carbon materials. *Carbon* **50**, 3376–3398 (2012).
- László, K., Bóta, A., Nagy, L. G. & Cabasso, I. Porous carbon from polymer waste materials. *Colloids Surf. A* **151**, 311–320 (1999).
- Li, Q., Yan, H., Cheng, Y., Zhang, J. & Liu, Z. A scalable CVD synthesis of high-purity single-walled carbon nanotubes with porous MgO as support material. *J. Mater. Chem.* **12**, 1179–1183 (2002).
- Che, G., Lakshmi, B. B., Martin, C. R. & Fisher, E. R. Chemical vapor deposition based synthesis of carbon nanotubes and nanofibers using a template method. *J. Mater. Chem.* **10**, 260–267 (1998).
- Chow, L. *et al.* Chemical vapor deposition of novel carbon materials. *Thin Solid Films* **368**, 193–197 (2000).



17. Reina, A. *et al.* Large area, few-layer graphene films on arbitrary substrates by chemical vapor deposition. *Nano Lett.* **9**, 30–35 (2009).
18. Li, X. *et al.* Large-area synthesis of high-quality and uniform graphene films on copper foils. *Science* **324**, 1312–1314 (2009).
19. Wei, D., Liu, Y., Wang, Y., Zhang, H., Huang, L. & Yu, G. Synthesis of N-doped graphene by chemical vapor deposition and its electrical properties. *Nano Lett.* **9**, 1752–1758 (2009).
20. Tabbal, M. *et al.* Effect of laser intensity on the microstructural and mechanical properties of pulsed laser deposited diamond-like carbon thin films. *J. Appl. Phys.* **85**, 3860–3865 (1999).
21. Zhang, H., Gu, H. & Iijima, S. Single-wall carbon nanotubes synthesized by laser ablation in a nitrogen atmosphere. *Appl. Phys. Lett.* **73**, 3827–3829 (1998).
22. Kong, X., Huang, Y. & Chen, Y. Difference in formation of carbon cluster cations by laser ablation of graphene and graphene oxide. *J. Mass Spectrom.* **47**, 523–528 (2012).
23. Saito, Y., Kawabata, K. & Okuda, M. Single-layered carbon nanotubes synthesized by catalytic assistance of rare-earths in a carbon arc. *J. Phys. Chem.* **99**, 16076–16079 (1995).
24. Qin, Z., Li, Z. J. & Yang, B. C. Synthesis of carbon nanowires as electrochemical electrode materials. *Mater. Lett.* **69**, 55–58 (2012).
25. Wen, F., Huang, N., Sun, H., Wang, J. & Leng, Y. X. Synthesis of nitrogen incorporated carbon films by plasma immersion ion implantation and deposition. *Surf. Coat. Technol.* **186**, 118–124 (2004).
26. Vizireanu, S., Stoica, S. D., Luculescu, C., Nistor, L. C., Mitu, B. & Dinescu, G. Plasma techniques for nanostructured carbon materials synthesis. A case study: carbon nanowall growth by low pressure expanding RF plasma. *Plasma Sources Sci. Technol.* **19**, 034016 (2010).
27. Lee, B., Kim, J. & Hyeon, T. Recent progress in the synthesis of porous carbon materials. *Adv. Mater.* **18**, 2073–2094 (2006).
28. Si, Y. & Samulski, E. T. Synthesis of water soluble graphene. *Nano Lett.* **8**, 1679–1682 (2008).
29. Dimovski, S., Nikitin, A., Ye, H. & Gogotsi, Y. Synthesis of graphite by chlorination of iron carbide at moderate temperatures. *J. Mater. Chem.* **14**, 238–243 (2004).
30. Wang, S. & Gao, Q. Synthesis, characterization and energy-related applications of carbide-derived carbons obtained by the chlorination of boron carbide. *Carbon* **47**, 820–828 (2009).
31. Koch, K., Bhushan, B. & Barthlott, W. Multifunctional surface structures of plants: an inspiration for biomimetics. *Prog. Mater. Sci.* **54**, 137–78 (2009).
32. Liu, C. Z. Biomimetic synthesis of collagen/nano-hydroxyapatite scaffold for tissue engineering. *J. Bionic Eng.* **5**, 1–8 (2008).
33. McKittrick, J. *et al.* Energy absorbent natural materials and bioinspired design strategies: A review. *Mater. Sci. Eng. C* **30**, 331–342 (2010).
34. Sailaja, G. S., Sreenivasan, K., Yokogawa, Y., Kumary, T. V. & Varma, H. K. Bioinspired mineralization and cell adhesion on surface functionalized poly(vinyl alcohol) films. *Acta Biomater.* **5**, 1647–1655 (2009).
35. Frackowiak, E. & Béguin, F. Carbon materials for the electrochemical storage of energy in capacitors. *Carbon* **39**, 937–950 (2001).
36. Lu, W., Hartman, R., Qu, L. & Liming, D. Nanocomposite electrodes for high-performance supercapacitors. *J. Phys. Chem. Lett.* **2**, 655–660 (2011).
37. Wu, F. C., Tseng, R. L., Hu, C. C. & Wang, C. C. Effects of pore structure and electrolyte on the capacitive characteristics of steam- and KOH-activated carbons for supercapacitors. *J. Power Sources* **144**, 302–309 (2005).
38. Wu, F. C., Tseng, R. L. & Hu, C. C. Comparisons of pore properties and adsorption performance of KOH-activated and steam-activated carbons. *Microporous Mesoporous Mat.* **80**, 95–106 (2005).
39. Wu, F. C., Tseng, R. L., Hu, C. C. & Wang, C. C. Effects of pore structure and electrolyte on the capacitive characteristics of steam- and KOH-activated carbons for supercapacitors. *J. Power Sources* **144**, 302–309 (2005).
40. Benaddi, H. *et al.* Surface functionality and porosity of activated carbons obtained from chemical activation of wood. *Carbon* **38**, 669–674 (2000).
41. Nian, Y. R. & Teng, H. Nitric acid modification of activated carbon electrodes for improvement of electrochemical capacitance. *J. Electrochem. Soc.* **149**, A1008–1014 (2002).
42. Cheng, P. Z. & Teng, H. Electrochemical responses from surface oxides present on HNO<sub>3</sub>-treated carbons. *Carbon* **41**, 2057–2063 (2003).
43. Nian, Y. R. & Teng, H. Influence of surface oxides on the impedance behavior of carbon based electrochemical capacitors. *J. Electroanal. Chem.* **540**, 119–127 (2003).
44. Wang, C. C. & Hu, C. C. Electrochemical catalytic modification of activated carbon fabrics by ruthenium chloride for supercapacitors. *Carbon* **43**, 1926–1935 (2005).
45. Wei, L., Sevilla, M., Fuertes, A. B., Mokaya, R. & Yushin, G. Hydrothermal carbonization of abundant renewable natural organic chemicals for high-performance supercapacitor electrodes. *Adv. Energy Mater.* **1**, 356–361 (2011).
46. Wei, L., Sevilla, M., Fuertes, A. B., Mokaya, R. & Yushin, G. Polypyrrole-derived activated carbons for high-performance electrical double-layer capacitors with ionic liquid electrolyte. *Adv. Funct. Mater.* **22**, 827–834 (2012).
47. Wang, D. W., Li, F., Liu, M., Lu, G. Q. & Cheng, H. M. Mesopore-aspect-ratio dependence of ion transport in rodtype ordered mesoporous carbon. *J. Phys. Chem. C* **112**, 9950–9955 (2008).
48. Wang, H., Gao, Q. & Jiang, L. Facile approach to prepare nickel cobaltite nanowire materials for supercapacitors. *Small* **17**, 2454–2459 (2011).
49. Fan, Z. *et al.* Template-directed synthesis of pillared-porous carbon nanosheet architectures: high-performance electrode materials for supercapacitors. *Adv. Energy Mater.* **2**, 419–424 (2012).
50. Li, Z. *et al.* Mesoporous nitrogen-rich carbons derived from protein for ultra-high capacity battery anodes and supercapacitors. *Energy Environ. Sci.* **6**, 871–878 (2013).
51. Shimodaira, N. & Masui, A. Raman spectroscopic investigations of activated carbon materials. *J. Appl. Phys.* **92**, 902–909 (2002).
52. Kim, H., Cho, J., Jang, S. Y. & Song, Y. W. Deformation-immunized optical deposition of graphene for ultrafast pulsed lasers. *Appl. Phys. Lett.* **98**, 021104 (2011).
53. Mhamane, D. *et al.* From graphite oxide to highly water dispersible functionalized graphene by single step plant extract-induced deoxygenation. *Green Chem.* **13**, 1990–1996 (2011).
54. Dresselhaus, M. S., Dresselhaus, G., Saito, R. & Jorio, A. Raman spectroscopy of carbon nanotubes. *Phys. Rep.* **409**, 47–99 (2005).
55. Wang, H., Gao, Q. & Hu, J. High hydrogen storage capacity of porous carbons prepared by using activated carbon. *J. Am. Chem. Soc.* **131**, 7016–7022 (2009).
56. Xu, H., Gao, Q., Guo, H. & Wang, H. Hierarchical porous carbon obtained using the template of NaOH-treated zeolite β and its high performance as supercapacitor. *Microporous Mesoporous Mat.* **133**, 106–114 (2010).
57. Wang, H., Gao, Q., Hu, J. & Chen, Z. High performance of nanoporous carbon in cryogenic hydrogen storage and electrochemical capacitance. *Carbon* **47**, 2259–2268 (2009).
58. Xia, K., Gao, Q., Jiang, J. & Hu, J. Hierarchical porous carbons with controlled micropores and mesopores for supercapacitor electrode materials. *Carbon* **46**, 1718–1726 (2008).
59. Chmiola, J., Yushin, G., Gogotsi, Y., Portet, C., Simon, P. & Taberna, P. L. Anomalous increase in carbon capacitance at pore sizes less than 1 nanometer. *Science* **313**, 1760–1763 (2006).
60. Wang, H. *et al.* Interconnected carbon nanosheets derived from hemp for ultrafast supercapacitors with high energy. *ACS Nano* **7**, 5131–5141 (2013).
61. Huang, W., Zhang, H., Huang, Y., Wang, W. & Wei, S. Hierarchical porous carbon obtained from animal bone and evaluation in electric double-layer capacitors. *Carbon* **49**, 838–843 (2011).
62. Elmouwahidi, A., Zapata-Benabith, Z. & Carrasco-Marín, F. Activated carbons from KOH-activation of argan (*Argania spinosa*) seed shells as supercapacitor electrodes. *Bioresour. Technol.* **111**, 185–190 (2012).
63. Li, Z. *et al.* Colossal pseudocapitance in a high functionality-high surface area carbon anode doubles the energy of an asymmetric supercapacitor. *Energy Environ. Sci.* **7**, 1708–1718 (2014).

## Acknowledgments

Financial supports by National Basic Research Programs of China (973 Programs, No. 2011CB935700 and 2014CB931800), Chinese Aeronautic Project (No. 2013ZF51069) and Chinese National Science Foundation (No. U0734002) are gratefully acknowledged.

## Author contributions

Q.-M.G. planned and supervised the project; L.J. and Q.-M.G. advised on the project; J.-D.X. and Q.-M.G. designed and performed experiments; J.-D.X., Y.-L.Z., Y.-L.T., W.-Q.T. and L.-H.Z. carried out the electrochemical property tests. Q.-M.G. and J.-D.X. analyzed data and wrote the manuscript; and all authors discussed the results and commented on the manuscript.

## Additional information

Supplementary information accompanies this paper at <http://www.nature.com/scientificreports>

**Competing financial interests:** The authors declare no competing financial interests.

**How to cite this article:** Xu, J. *et al.* Preparing two-dimensional microporous carbon from Pistachio nutshell with high areal capacitance as supercapacitor materials. *Sci. Rep.* **4**, 5545; DOI:10.1038/srep05545 (2014).



This work is licensed under a Creative Commons Attribution-NonCommercial-NoDerivs 4.0 International License. The images or other third party material in this article are included in the article's Creative Commons license, unless indicated otherwise in the credit line; if the material is not included under the Creative Commons license, users will need to obtain permission from the license holder in order to reproduce the material. To view a copy of this license, visit <http://creativecommons.org/licenses/by-nc-nd/4.0/>